Petroleum Science 23 (2026) 2263–2274

Contents lists available at ScienceDirect

Petroleum Science

journal homepage: www.keaipublishing.com/en/journals/petroleum-science

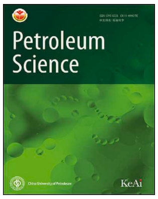

Original Paper

Seepage and blockage characteristics of methane hydrate-bearing porous media under different hydrate distribution conditions

Guo-Jun Zhao [a,b], Jia-Nan Zheng [c,d,*], Ming-Jun Yang [a,**], Yong-Chen Song [a]

[a] Key Laboratory of Ocean Energy Utilization and Energy Conservation of Ministry of Education, Dalian University of Technology, Dalian, 116024, Liaoning, China
[b] Department of Mining Engineering, Taiyuan University of Technology, Taiyuan, 030024, Shanxi, China
[c] Shanghai Institute for Advanced Study, Zhejiang University, Shanghai, 201203, China
[d] Department of Civil Engineering, Shanghai University, Shanghai, 200444, China

ARTICLE INFO

Article history:
Received 5 May 2025
Received in revised form
5 September 2025
Accepted 16 November 2025
Available online 21 November 2025

Edited by Teng Zhu and Min Li

Keywords:
Methane hydrate
Distribution difference
Formation kinetic
Porous media permeability
Seepage and blockage

ABSTRACT

Blockage commonly occurs in and severally affects natural gas (mainly methane) reservoir exploitation, combustion ice (methane hydrate) exploitation and oil and gas pipeline transportation. The formation of methane hydrates is known as one important cause of blockage, but the effects of hydrate distribution on seepage and blockage are rarely studied in experiments. This study employed different proportions of dry and wet sands to simulate three thickness of hydrate-bearing porous media and obtained a uniform kinetic relationship of hydrate formation ($N = K\left(1 - \frac{1}{e^{rt}}\right)$). Quantitative results indicate that both water and methane seepage can induce hydrate saturation increase in both hydrate-bearing and hydrate-free zones, which gradually causes the blockage of up to 12.5 MPa (at 6.0 MPa backpressure). The hydrate-bearing porous media with a uniform saturation is not easy to cause blockage unless the hydrate saturation is high enough. In addition, based on the hydrate-bearing porous media with different thicknesses, this study successively measured the water phase permeability. In addition, the calculation method for blockage location based on pressure evolution was proposed with an error of less than 8%. These findings can help understand and mitigate issues related to flow blockages during oil and gas exploitation and transportation.

1. Introduction

Nowadays, global natural gas (mainly methane) production has reached more than 4.28 trillion cubic meters (Wang et al., 2022). When environmental temperature is low such as deep sea, permafrost regions or severe winter, the formation of methane hydrates is highly likely during both exploitation and transportation processes (Song et al., 2022; Feng et al., 2024). In marine sediments, methane hydrate is typically formed when methane gas encounters pore water under favorable thermodynamic conditions, leading to the crystallization of methane-water clathrate structures (Zheng and Yang, 2019). It is revealed that shallow gas reservoirs are often present beneath natural gas hydrate reservoirs (Wei et al., 2022a), and this composite-type gas hydrate reservoir has higher exploitation potential and research value (Ren et al., 2022). The presence of methane hydrate in oceanic sediments has significant implications for global energy security, and climate change.

The formation of hydrate within oceanic sediments is influenced by various factors, including sediment composition, initial water distribution, and methane migration pathways (Sakurai et al., 2021; Farhadian et al., 2022; Zhang et al., 2023b). One of the fundamental aspects of methane hydrate formation is the upward migration of methane gas through the thermodynamic

---

* Corresponding author.
** Corresponding author.
E-mail addresses: zhengjn@zju.edu.cn, jia-nan_zheng@shu.edu.cn (J.-N. Zheng), yangmj@dlut.edu.cn (M.-J. Yang).
Peer review under the responsibility of China University of Petroleum (Beijing).

https://doi.org/10.1016/j.petsci.2025.11.028

stability zone of hydrate (Fu et al., 2021). The formation of hydrates begins with two requirements: phase equilibrium conditions and disturbance at the gas-water interface (Xu et al., 2023). Song et al. (2015), Wang et al. (2017, 2018) systematically investigated the characteristics of hydrate formation during methane flow. Their study found that gas migration enhances mass transfer efficiency between gas and water, leading to increased gas dissolution and promoting hydrate formation. However, due to limitations in gas-water contact area and pressure-temperature conditions, the phenomenon of hydrate formation decrease during gas flow may occur as reservoir water saturation increases.

It is well known that hydrate formation significantly reduces reservoir permeability (Zhang et al., 2023c). Zhang et al. (2024a; 2024b) measured the hydrate saturation using time domain reflectometry method and X-ray computed tomography techniques, the hydrate formation process was more accurately reproduced to reveal the impact of hydrate formation on reservoir permeability. Zhang et al. (2023a) found that the intersections of different pore channels were key locations for hydrate blockage in the micro-model, the higher the pressure in the pore channels, the greater the risk of hydrate formation and blockage. Hydrate blockage is the fundamental mechanism leading to the accumulation of shallow gas beneath hydrate reservoirs (Bohrmann et al., 2023). Sun et al. (2023) studied the characteristics of hydrate reformation during the seepage flow process and found that a lower effective water cross-sectional velocity reduces the gas concentration gradient between water and hydrate, thereby enhancing hydrate reformation. However, in recent decades, extensive research was conducted to understand the thermodynamic and kinetic mechanisms of methane hydrate formation in static system (Chibura et al., 2022), It is necessary to study the characteristics of hydrate formation in dynamic systems and the influence on reservoir permeability.

During hydrate exploitation, the dynamic behavior of gas-water flow within hydrate-bearing sediments is crucial for determining reservoir performance (Ji et al., 2022). Gas production from hydrate reservoirs typically involves depressurization (Lee et al., 2020), thermal stimulation (Ma et al., 2024), chemical injection (Yu et al., 2021), or CO_2 replacement methods (Wei et al., 2022b), all of which induce fluid migration within the sediment matrix (Ye et al., 2025). Zhao et al. (2025b) investigated the co-production of gas hydrate and high-pressure underlying gas by depressurization method, they found that due to the rapid increase in the contact area between gas and water, the free gas from shallow gas zone enhanced the reformation of hydrate in the hydrate stability zone. Guo et al. (2025) studied the effect of interlayer flow capacity on hydrate co-production using numerical simulations and proposed a logarithmic regression model that reflects the impact of cross-flow gas on hydrate dissociation under different interlayer flow rates. Chen et al. (2019, 2021), Li et al. (2020) experimentally investigated the effect of undersaturated aqueous solutions on hydrate dissociation and explained the promotion mechanism based on the fugacity difference between water and hydrate. On this basis, Sun et al. (2020a; 2020b) proposed a water injection-assisted depressurization method for hydrate exploitation, significantly improving both extraction efficiency and safety. The gas-water flow characteristics in hydrate-bearing sediments play a crucial role in controlling hydrate distribution, reservoir permeability, and hydrate dissociation efficiency during exploitation (Marques et al., 2022).

In the experimentally studied sediment layers with a uniform distribution, hydrate formation during the gas flow process is highly likely to induce the development of a hydrate-sealing cap (Zhao et al., 2022b, 2023b). However, in real marine sediment environments, hydrate distribution is highly heterogeneous due to variations in sediment permeability, pore size distribution, and initial water saturation (Gong et al., 2023b). This heterogeneity directly affects the gas-water migration pathways, leading to complex flow dynamics that influence both hydrate formation and dissociation (Kou et al., 2022). Ji et al. conducted *in situ* measurements of methane hydrate formation and permeability in sandstone using the low-field nuclear magnetic resonance measurement system, they found that the heterogeneity of methane hydrate distribution significantly affects the analysis of permeability changes in the sediment layer (Ji et al., 2020). Zhang et al. constructed a heterogeneous sediment particle distribution model, accurately describing the particle size distribution of water-bearing core samples collected from the Nankai Trough in Japan (Zhang et al., 2022).

However, there is few researches on hydrate formation and gas-water flow characteristics in sediment layers with different water distributions. In this study, experimental methods were used to simulate the hydrate formation process in sediment layers with varying water distributions. On this basis, the gas-water flow characteristics in hydrate-bearing sediment layers with heterogeneous distribution were investigated. The insights gained from this research contribute to the mechanism of hydrate formation and the development of more efficient and sustainable strategies for exploiting natural gas hydrate resources.

2. Experimental methods

2.1. Apparatus and materials

Fig. 1 illustrates the assembled experimental apparatus, which primarily comprised a high-pressure vessel, a gas-liquid separator, several pressure control valves, a gas collector, a mass balance, an ISCO pump, two thermostatic water baths, three temperature sensors, three pressure transducers, and a data acquisition unit. The high-pressure vessel (Φ 50 × 235 mm) served as the vessel and was filled with BZ-01 glass beads to simulate uniform marine sediments. The particle diameter of BZ-01 glass beads is 0.105–0.125 mm, the porosity of BZ-01 glass beads obtained by experimental measurement is 34.8% (Yang et al., 2015), the density of BZ-01 glass beads obtained by experimental measurement is 1.45 g/cm^3 (Sun et al., 2023). The high-pressure vessel had a maximum pressure endurance of 15 MPa and was submerged in a temperature-controlled water tank, which also housed the water source to ensure stable experimental conditions.

The water injection pump offered a flow control accuracy of 0.01 mL/min and a pressure control precision of ±0.5%, while the ISCO pump, used for gas injection, achieved a finer flow control of 0.001 mL/min with the same pressure accuracy, and the volume error of the ISCO pump is ±0.001 mL. A separate water bath regulated the gas temperature. Three high-precision (±0.05%) pressure transducers were installed at the vessel inlet, outlet, and gas collector, while three temperature sensors (±0.05 °C accuracy) were spaced along the vessel for thermal measurements. A computer, interfaced via an A/D module, recorded temperature, pressure, and mass balance data. The experiment utilized deionized water, and the methane gas (99.99% purity) was sourced from Dalian Special Gases Company.

2.2. Experimental procedure

This study systematically investigated the formation process of gas-saturated hydrate within sediment layer with different pore water distributions, the pore water flow process within sediment layer in different hydrate distribution zones, and the gas flow

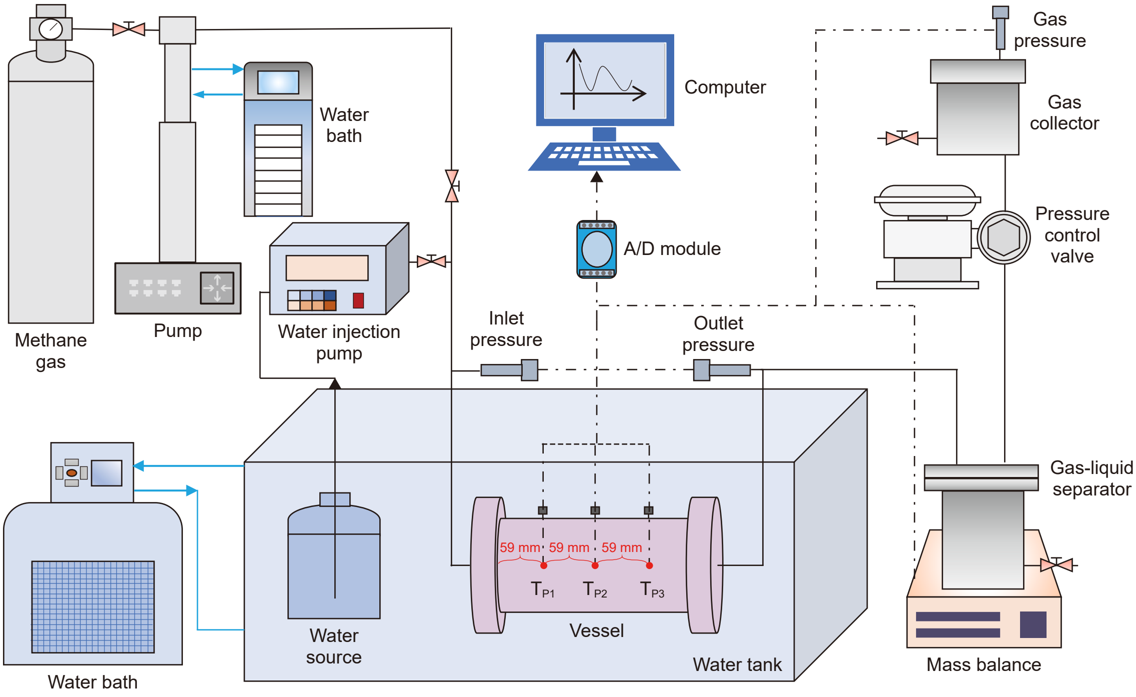

Fig. 1. Schematic diagram of the experimental apparatus.

process within hydrate-bearing sediment layers, as shown in Fig. 2.

(1) Hydrate formation process

First of all, according to the experimental design, glass sand with an initial water saturation of 40% and dry glass sand were proportionally packed into the vessel. For Case 1, 25% of the vessel volume was first filled with glass sand with 40% initial water saturation, based on the density of BZ-01 glass beads, 167 g of glass beads were required. According to the porosity of BZ-01 glass beads, the required volume of deionized water was calculated to be 16 mL. The deionized water was thoroughly mixed with the glass beads to obtain wet sand with an initial water saturation of 40%. Then, 75% of the volume filled with 501 g dry glass sand. For Case 2, 50% of the vessel volume was filled with water-saturated glass sand, and the other 50% with dry glass sand to simulate a sediment region with a moderate pore water distribution. For Case 3, the vessel was entirely filled with water-saturated glass sand to simulate a sediment region with a large pore water distribution. The specific ratios of water-saturated glass sand to dry glass sand are shown in Table 1.

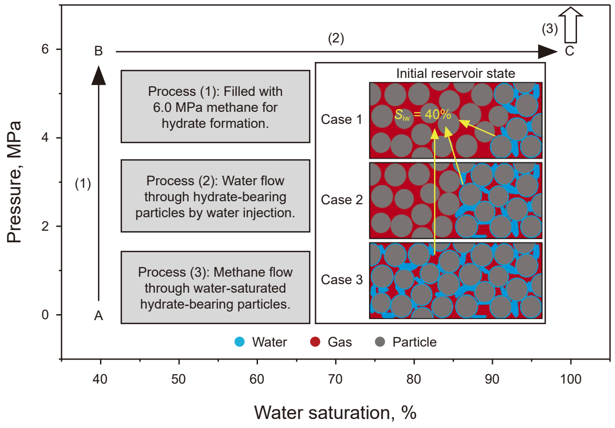

Fig. 2. Experimental process of water and gas flow in different water-containing sediments.

After compactly packing the glass sand into the vessel, the outlet valve of the vessel was closed, and the vessel inlet was connected to the gas injection pump. Methane gas was then injected into the vessel, and a constant pressure of 6.0 MPa was maintained by the pump (process A–B in Fig. 2). The vessel temperature was controlled at 1 °C using the water bath to. The real-time hydrate formation amount (n_H) can be calculated using Eq. (1):

$$n_H = \frac{P \cdot V}{Z \cdot R \cdot T} \tag{1}$$

where P, T represent the internal pressure and temperature of the vessel, respectively. V represents the gas consumption. The compressibility factor of methane (Z) can be determined using the Redlich-Kwong (R-K) equation (Li et al., 2019). The hydrate saturation (S_H) can be calculated using Eq. (2):

$$S_H = \frac{n_H \cdot M_H}{V_p \cdot \rho_H} \tag{2}$$

where V_p represented the pore volume of the vessel, and $V_p =$ 160.08 mL. M_H represented the molar mass of methane hydrate, $M_H = 124$ g/mol, ρ_H represented the density of methane hydrate, $\rho_H = 0.94$ g/cm^3 (Sun et al., 2021).

(2) Water flow process through hydrate-bearing sediments

After hydrate formation was completed, the back-pressure valve was adjusted to match the vessel pressure at 6.0 MPa. The vessel outlet valve was then opened, while the valve between the gas injection pump and the vessel was closed. Subsequently, the

Table 1
Basic information on initial reservoir condition.

Case	Wet sand				Dry sand		
	Proportion	Thickness, mm	Water, mL	Glass beads, g	Proportion	Thickness, mm	Glass beads, g
1	25%	58.75	16	167	75%	176.25	501
2	50%	117.5	32	334	50%	117.5	334
3	100%	235	64	668	0%	0	0

water injection pump was opened, allowing water to be continuously injected into the gas-saturated hydrate-bearing sediment layer at a rate of 1.7 mL/min to simulate the water flow process (process B-C in Fig. 2). During this process, the real-time hydrate formation amount can still be calculated using Eq. (1), where the gas consumption V in the vessel was determined by the difference between the influx and efflux gas volumes. Once the water flux at the inlet and outlet of the vessel stabilized, the permeability of the sediment layer can be calculated using Eq. (3)(Wang et al., 2024):

$$K_{\mathrm{ew}} = \frac{Q_{\mathrm{w}} \cdot \mu \cdot L}{\Delta P \cdot A_{\mathrm{s}}} \tag{3}$$

where K_{ew} represents the water effective permeability, mD; Q_{w} represents the water flow rate, mL/min; μ represents the dynamic viscosity of water, mPa·s; L represents the length of the vessel, cm; ΔP represents pressure difference between the vessel inlet and outlet, respectively; and A_{s} represents the cross-section of the vessel, cm^2.

(3) Gas flow process through water-saturation hydrate-bearing sediments

Once the water flow stabilizes and the inlet and outlet flow rates remained consistent, the sediment layer can be considered in the water-saturation state. At this point, the water injection pump was closed, while the gas injection pump was opened. The gas injection rate was adjusted to 6 mL/min to simulate gas flow through the water-saturated hydrate-bearing sediment zone. During this process, the real-time hydrate formation amount can still be calculated using Eq. (1), where the gas consumption V in the vessel was determined by the difference between the influx and efflux gas volumes.

3. Results and discussion

Whether in the formation or exploitation of natural gas hydrate, gas-water flow in porous media is inevitably involved. This study investigated the entire process of hydrate formation and gas-water flow within sediment zones with different water distribution. The experimental conditions were set at a sediment temperature of 274.15 K and a pressure of 6.0 MPa.

3.1. Methane hydrate formation characteristics in porous media with different thicknesses

In deep marine sediments, thermogenic and biogenic gases migrate, and when methane encounters pore water under suitable temperature and pressure conditions, hydrate formation occurs (Fu et al., 2021). Due to permeability variations in the sediment layers, pore water distribution is ununiform. Thus, this study investigated the characteristics of hydrate formation in different water distribution zones. It should be to emphasize that the initial water saturation within the water-bearing regions was consistent across all cases, maintained at 40%.

Due to variations in the initial water distribution, this study aims to obtain hydrate-bearing sediment zones with the same hydrate saturation. The hydrate formation amount is positively correlated with the initial water distribution pattern, and the formation process was completed once the target hydrate saturation was reached. The real-time hydrate formation process is shown in Fig. 3. At the beginning, the hydrate amount remained zero because this was in the induction process of hydrate formation. The induction exhibited a degree of randomness, because hydrate formation requires the formation of a critical nucleus, this process is influenced by random molecular collisions, and the uneven distribution of pore water within the sediment, the local fluctuations in pressure and temperature within the sediment layer further affect hydrate formation (Lv et al., 2025). The relationship between the hydrate formation rate and the hydrate formation amount was further analyzed, as shown in Fig. 4(a). The hydrate formation rate gradually decreased with hydrate formation and exhibited a negative correlation. Thus, the hydrate formation rete can be expressed as Eq. (4):

$$\frac{\mathrm{d}N}{\mathrm{d}t} = r(K - N) \tag{4}$$

where N represents the real-time hydrate formation amount, mol; r is the proportionality constant of hydrate formation rate, min^{-1}; K is the hydrate formation constant. Thus, after integration, the real-time hydrate formation can be expressed as Eq. (5):

$$N = K\left(1 - \frac{1}{\mathrm{e}^{rt}}\right) \tag{5}$$

The values of r and K in each case is summarized in Table 2. In addition, the average absolute relative error (AARE) can be calculated by Eq. (6):

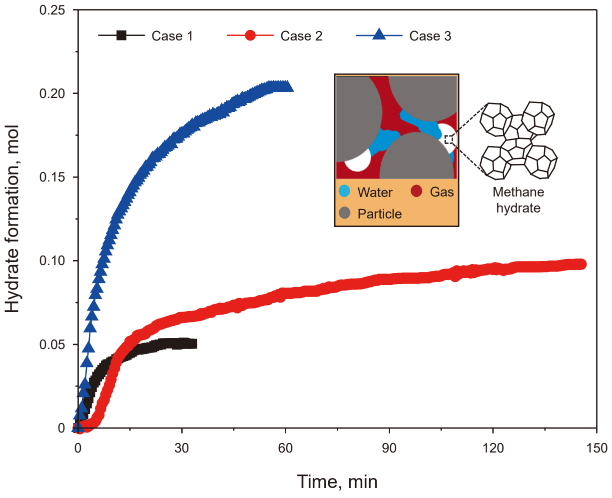

Fig. 3. Hydrate formation in different water distribution zones.

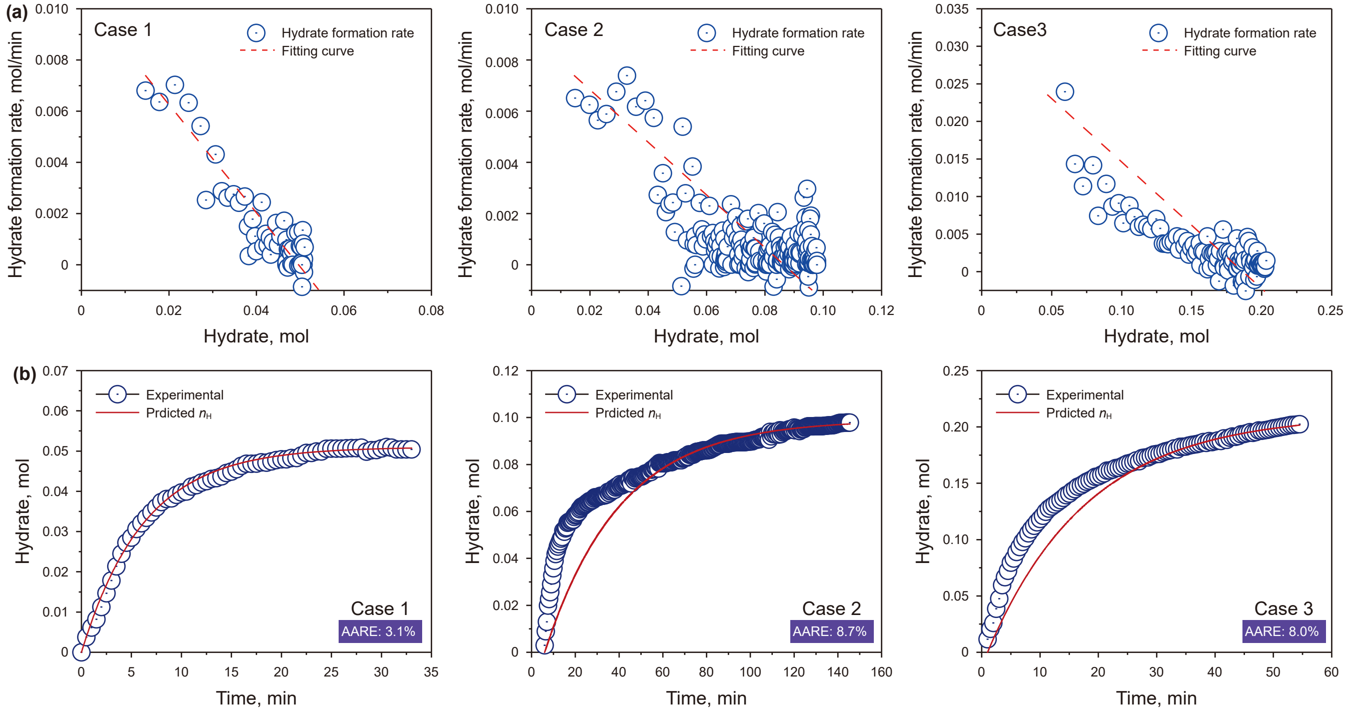

Fig. 4. Real-time hydrate formation rate (**a**) and comparison of real-time hydrate formation between actual values with expected values (**b**) in different cases.

Table 2
Values of constants and AARE in each case.

Case	r, min^{-1}	K	AARE, %
1	0.160	0.051	3.1
2	0.029	0.099	8.7
3	0.058	0.211	8.0

$$\text{AARE} = \left(\frac{1}{N_\text{P}} \sum_{i=1}^{N_\text{P}} \frac{\left| P_i^{\text{exp}} - P_i^{\text{model}} \right|}{P_i^{\text{exp}}} \right) \times 100\% \tag{6}$$

The comparison of hydrate formation in porous media between experimental values with predicted values are shown in Fig. 4(b). The differences in hydrate distribution among the cases, variations in the contact area between water and hydrate, and local pressure differences in different regions of the sediments can also lead to variations in hydrate formation rates, thereby affecting the accuracy of the model and causing the noticeable discrepancies especially in cases 2 and 3. This model provides an initial method for calculating hydrate formation and aligns with the kinetic characteristics of hydrate formation, but it still requires further refinement. The model exhibits a good fit with the actual hydrate formation process, with an *AARE* of less than 9% in this study. Thus, this model is applicable for predicting hydrate formation within sediment particles containing pore water. However, it remains a fundamental model, as the proportionality constant *r* and constant *K* are influenced by factors of hydrate formation, such as environmental temperature, pressure, porous media type, pore water distribution, and water saturation, and so on, the values of *r* and *K* still require further investigation.

Fig. 5(a) demonstrates the temperature variation patterns within the sediment zone at different locations. Hydrate formation is an exothermic process (Dong et al., 2025), leading to an increase in reservoir temperature. Therefore, temperature changes can be used to determine the regions where hydrate formation occurred. It can be found that the temperature increases and duration varied at each measurement point, and the increase in temperature followed by a sustained high-temperature phase indicated continuous hydrate formation. A longer duration of high temperature indicated a longer hydrate formation duration. This can be used to determine the specific location of the measurement points. Fig. 5(b) demonstrates the temperature increase and duration of mean hydrate formation in different locations. The temperature increase and duration at measurement point T_{P3} were relatively long in every Case because T_{P3} was located in a water-containing zone, where the heat released from hydrate formation was contacted to the measurement point. In contrast, in Case 2, the temperature increase and duration at T_{P2} were significantly shorter. This was because T_{P2} in Case 2 was located in the zone with no pore water but was close to the pore water-containing zone, where heat transferred from hydrate formation led to the temperature increase.

3.2. *Effects of hydrate layer thickness on seepage characteristics of hydrate-bearing porous media*

The exploitation process of gas hydrate also involves significant pore water migration within hydrate-bearing sediment zones. However, in real marine sediments, hydrates exhibit a heterogeneous distribution (Li et al., 2025). Therefore, the effect of pore water flow on the reservoir with different hydrate distribution was investigated.

Fig. 6(a) demonstrates the pressure changes at the vessel inlet, while the outlet pressure remains constant at 6000 kPa. It was found that as pore water flowed through the hydrate-bearing zones, the inlet pressure increased. This was due to two primary reasons: one was that hydrate formation occupied pore space, and the effective pore radius was reduced. The capillary pressure (ΔP_c) between the pore water with hydrate increased, as shown in Young-Laplace equation: $\Delta P_c = 2\gamma(1/r_1 - 1/r_2)$, where r_1 and r_2

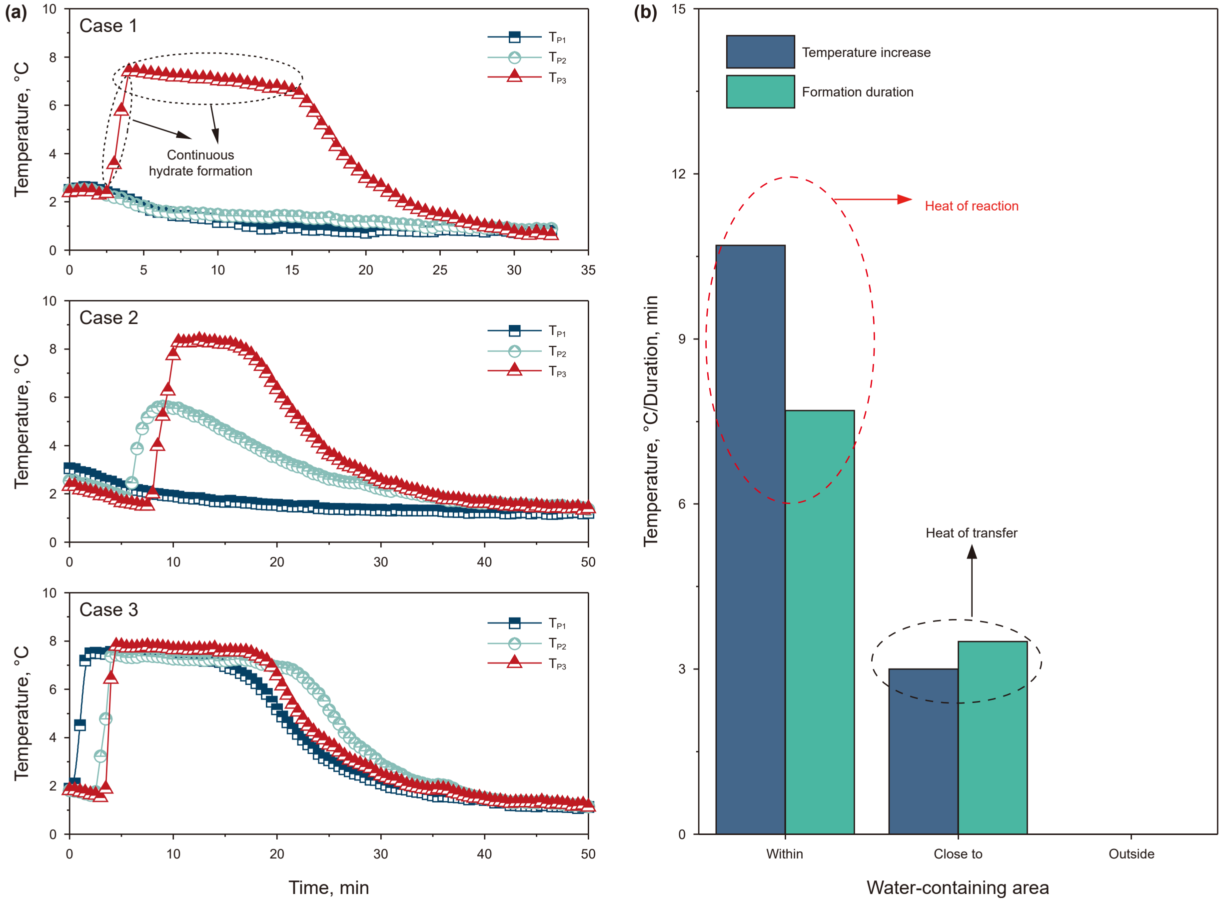

Fig. 5. Real-time temperature changes (**a**) and duration of mean hydrate formation in different locations (**b**).

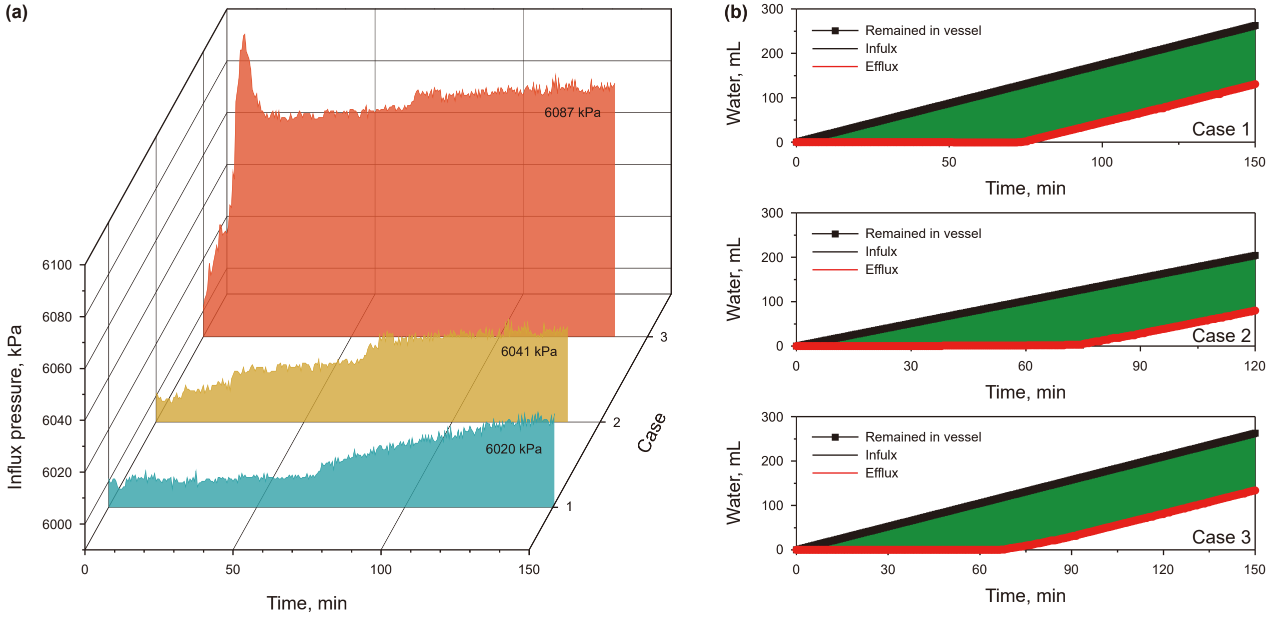

Fig. 6. Real-time pressure (**a**) and flux (**b**) changes during water flow process.

are the effective pore radius of small and large pores (Zhao et al., 2023a), and the capillary pressure impeded pore water movement and created a pressure difference. The other was that gas hydrates are hydrophilic (Zhao et al., 2022a), which further hindered water flow. In Case 1, a significant increase in inlet pressure occurred after 70 min, as the hydrate-bearing zone was located farther from the initial water flow position. In contrast, in Case 3, the pressure rise occurred immediately at the onset of flow, as hydrate were distributed throughout the entire sediment zone. However, after the initial pressure increase, a sudden decrease was observed, indicating a local breakthrough phenomenon. This occurred when the inlet pressure exceeded the capillary pressure exerted by the confined pore water, causing a rapid pressure drop. As water continued flowing, the pore space eventually becomes fully saturated, and excess water began to efflux from the vessel outlet. As shown in Fig. 6(b), when the water flowed out of the vessel, the efflux of outlet water became parallel to the influx of inlet water, indicating that the influx and efflux reached equilibrium. Thus, it can be assumed that the flow of water in a porous medium occurs in the form of an interface and is perpendicular to the flow direction. In addition, the sediment zone was considered to be in a water-saturation state, and the stable water flow provided the basis for permeability calculations.

Although hydrate formation in water-saturation zones occurred at a slow rate, some researchers even neglected (Zhao et al., 2017), pore water flowing into the sediment interacted with the pre-existing methane gas in the pore space, leading to hydrate formation during water flow process. Before the water flow, the sediment layer was divided into hydrate-bearing zone and hydrate-free zone. In Case 3, the hydrate was uniformly distributed along the vessel, and the point when the water efflux increased from zero was considered the time when the water flow interface reached the outlet. Based on this, the movement speed of the water interface in the hydrate-bearing zone was calculated to be 3.4 mm/min. Similarly, the interface movement speeds in the hydrate-free zones of Cases 1 and 2 can be calculated, the results were shown in Table 3. Based on this, the time when the interface arrived in different positions can be determined, while the time when the temperature increases was corresponding to the hydrate formation point, as shown in Fig. 7(a)–(c). By comparing these two points, it can be found that in the hydrate-free zone, hydrate formation occurred after the water interface had passed, because the movement of the interface brought in pore water, which reacted with the residual gas in the pores to form hydrate. In contrast, in the hydrate-bearing zone, hydrate formation occurred before the interface passed, due to the presence of residual water in the hydrate-bearing zone, where water flow induced gas movement in the pores, increasing disturbances and promoting hydrate formation. In addition, the T_{P2} in Case 2 was located in the middle of the vessel but closer to the hydrate-free zone. However, the temperature increase still occurred before the water interface passed. This was attributed to the exothermic reaction from the substantial hydrate formation near T_{P2}, with the resulting heat transfer leading to the observed temperature rise.

To calculate permeability, it is necessary to determine the hydrate distribution during the water injection process. During the water flow process, hydrate formation in the hydrate-bearing zone was considered reformation, while hydrate formation in the hydrate-free zone was considered first formation, as shown in Fig. 8(a). Assuming that the hydrate reformation and hydrate first formation was equally distributed in the hydrate-bearing zone and the hydrate-free zone, respectively, the mean hydrate distribution along the vessel length (235 mm) can be calculated by Eq. (7):

$$\Delta n_{\mathrm{H}} = L_{\mathrm{HB}} \cdot D_{\mathrm{HB}} + L_{\mathrm{HF}} \cdot D_{\mathrm{HF}} \tag{7}$$

where L_{HB} and L_{HF} are the length of hydrate-bearing zone and hydrate-free zone, respectively, mm; D_{HB} and D_{HF} are the distribution of hydrate reformation in hydrate-bearing zone and hydrate formation in hydrate-free zone, respectively, mol/mm. D_{HB} can be obtained from Case 3. The hydrate reformation along the vessel in Cases 1, 2 was the same with Case 3. Based on this, D_{HF} in Cases 1 and 2 can be calculated through Eq. (7). It should be emphasized that the error in this calculation mainly caused by the uneven distribution of hydrate, and the inhomogeneity of hydrate distribution is the error of Eq. (7). Thus, the hydrate distribution at different positions within each case after water flow can be obtained, as shown in Fig. 8(b).

The hydrate saturation in hydrate reformation zone was higher than that in the zone of hydrate first formation. Thus, when calculating permeability using Eq. (3), the values of L in different cases were assigned as follows: $L_1 = L/4$ (1/4 of the vessel length) in Case 1, $L_2 = L/2$ in Case 2, and $L_3 = L$ in Case 3. The resulting permeability values are shown in Fig. 8(c). It can be found that the permeability values were very similar in each Case. This was because the permeability was primarily determined by zones with high hydrate saturation (Gong et al., 2023a), and it also indirectly confirmed that the hydrate saturation in the hydrate reformation zones was very similar across all cases.

3.3. Blockage characteristics of saturated porous media with different hydrate thicknesses

Gas flow within hydrate-bearing sediment zone is a more prevalent phenomenon (Yin et al., 2018). This study investigated the changes of sediment layer state during gas flow based on the water-saturation hydrate-bearing sediment, and the gas flow rate was 6 mL/min. The most significant change was the reservoir pressure. As shown in Fig. 9(a)–(c), the inlet pressure of the reservoir reached a maximum of 12,500 kPa, indicating that hydrate-bearing reservoirs imposed a significant blockage. Compared to the water flow process, the gas flow process generated a more significantly larger pressure difference. As gas entered the sediment layer, part of it displaced pore water and occupied the pore space, while another portion reacted with water to form hydrates, and the remaining gas flowed out through the outlet. A comparison of methane and water efflux revealed that at the beginning of gas flow, the water efflux increased significantly, while the methane efflux remained at zero, which indicated that the process initially involves gas displacing pore water. By calculating the difference between the gas influx and efflux, the real-time hydrate formation amount during gas flow can be determined. In Case 1, the gas flux remained stable even after the inlet pressure reached its peak, indicating that complete blockage occurred in the sediment layer. In contrast, in Cases 2 and 3,

Table 3
Results of water interface movement in different cases.

Case	Interface migration duration, min		Interface migration rate, mm/min	
	In hydrate-bearing zone	In hydrate-free zone	In hydrate-bearing zone	In hydrate-free zone
3	68	0	/	3.45
2	34	38	3.09	3.45
1	17	57	3.09	3.45

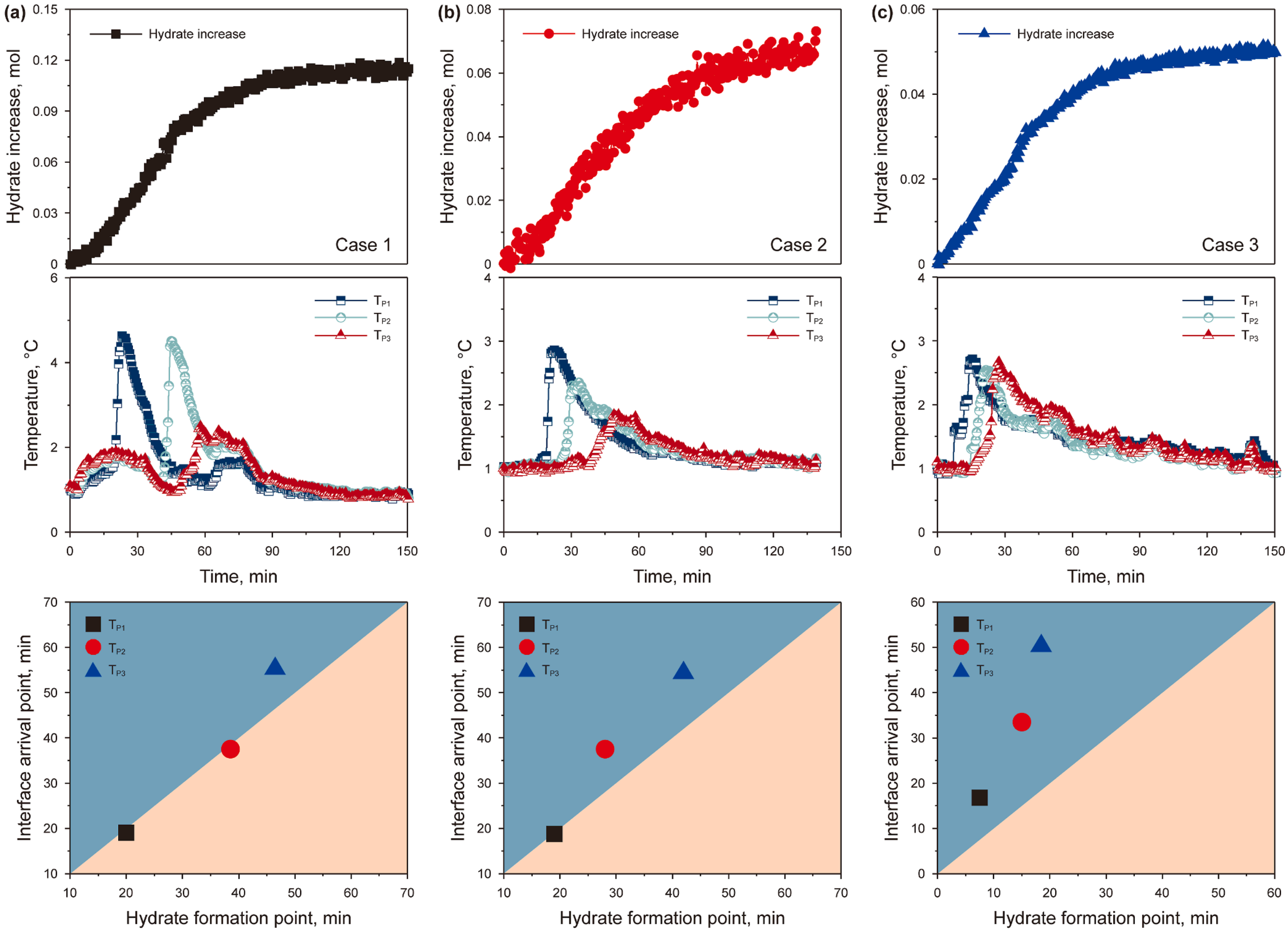

Fig. 7. Hydrate formation and temperature changes during water flow process.

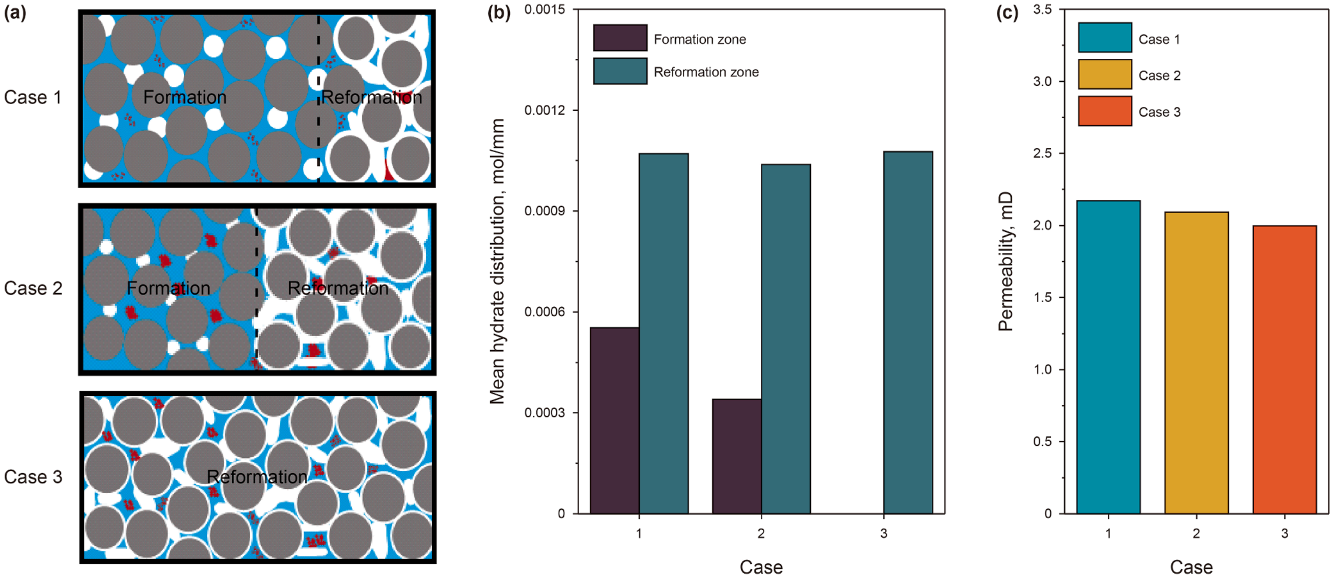

Fig. 8. Schematic diagram of hydrate formation (**a**), mean hydrate distribution in different zones (**b**) and reservoir permeability (**c**) during water flow process.

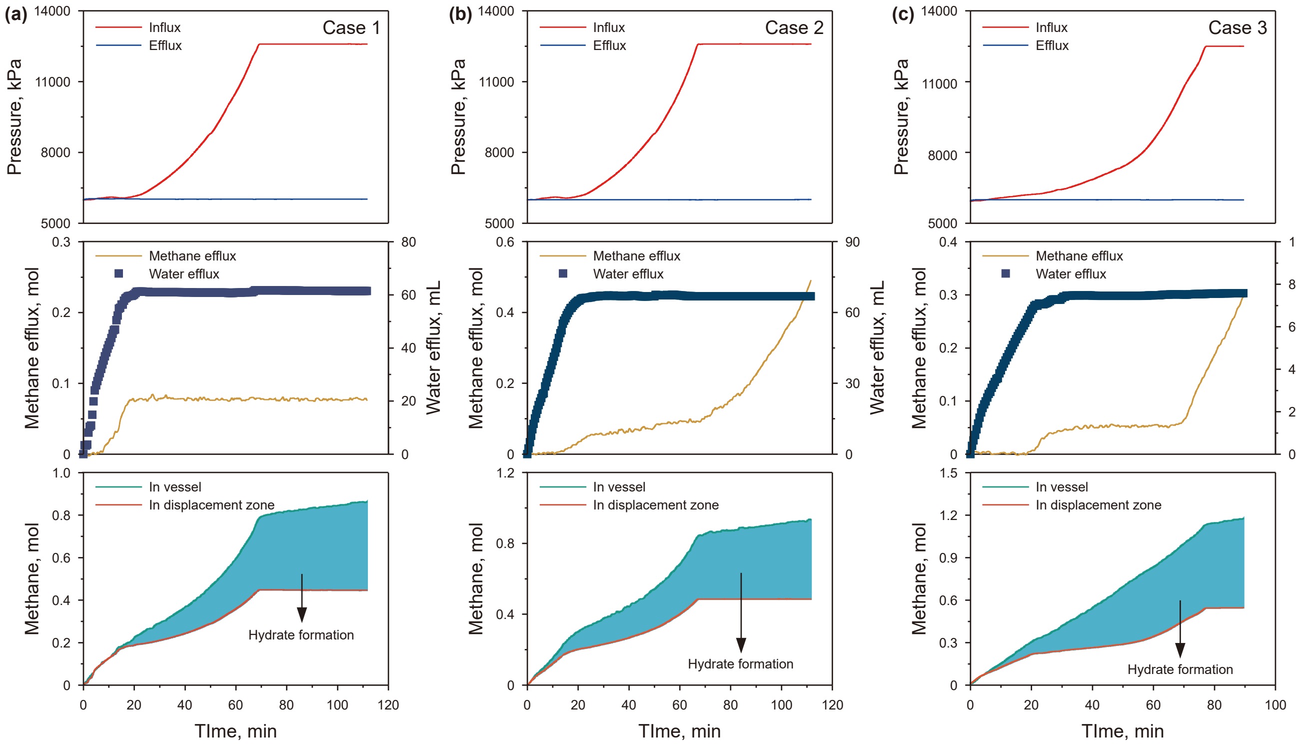

Fig. 9. Reservoir state during gas flow process in Case 1 (**a**), Case 2 (**b**), and Case 3 (**c**).

methane outflow increased significantly after the inlet pressure reached its maximum, while the inlet pressure itself has not dropped abruptly, this suggested that local breakthrough occurred within the sediment layer due to high-pressure gas overcoming the capillary sealing in certain pore channels (Zhao et al., 2025a).

Fig. 10 demonstrates the temperature changes at different locations during gas flow process, where the point that the temperature began to increase was corresponded to the onset of hydrate formation at each location. Similarly, the movement of the gas-water interface can be determined based on the water efflux in Fig. 9. The point when the water efflux stabilizes marked the point when the interface reached the vessel outlet, allowing the calculation of the interface movement rate and the time required for the interface to reach different positions. By comparing the time for the interface to reach different positions with the onset time of hydrate formation (as shown in Fig. 10), it was found that hydrate formation occurred after the interface arrived. This is because the area ahead of the interface was water-saturated, while the area behind the interface had been displaced, leading to gas-water contact and subsequent hydrate formation. In addition, the time difference between the interface arrival and hydrate formation at different positions represented the induction time for hydrate reformation during the flow process, which exhibited randomness. Hydrate formation occurred after the gas displaced water, leading to changes in the pore structure within the sediment layer. The pore water generated larger capillary forces in the narrower spaces, blocking the gas flow.

After gas-driven water displacement ended (water efflux stabilized), the inlet pressure of the sediment layer increased significantly, indicating the existence of hydrate blockage. The end of displacement served as the onset signal of blockage. Once blockage occurred, the pressure increase was caused by the continuous gas inflow, and the mass of the blocked gas (m_g) can be calculated as Eq. (8):

$$m_{\mathrm{g}} = n_{\mathrm{g}} \cdot M_{\mathrm{CH_4}} = \rho_{\mathrm{i}} \cdot (V_{\mathrm{i}} + V_{\mathrm{B}}) \tag{8}$$

where ρ_{i}, V_{i} are the initial density and volume in the pump of the CH_4 that is blocked by the hydrate blockage, respectively; V_{B} is the volume of blocked CH_4 in the vessel, mL. As the gas was continuously injected into the vessel, the V_{i} was decreasing, the real-time volume blocked CH_4 in the pump was represented through V_t. Thus, the relationship between V_{B} and the real-time pressure of blocked CH_4 can be expressed by Eqs. (9) and (10):

$$\rho_t = \frac{m_{\mathrm{g}} - n_{\mathrm{l}} \cdot M_{\mathrm{CH_4}}}{V_t + V_{\mathrm{B}}} \tag{9}$$

$$P_t = F(\rho_t, T) \tag{10}$$

where n_{l} represent the leaked CH_4 through the vessel outlet, mol. By substituting the reservoir pressure and temperature at the final moment of the pressure increase caused by blockage into Eq. (10), the value of V_{B} can be calculated. Then, this calculated V_{B} can be substituted back into Eqs. (9) and (10) to compute the pressure variations at different moments caused by the blockage. By comparing the calculated pressure values P_t with the experimental data, the calculation error can be determined, as shown in Fig. 11.

The error in Case 3 was relatively large because the V_{B} increased due to the local breakthrough within the sediment after displacement. The formation of hydrate during gas flow changed the pore structure, leading to changes in V_{B}, which was a key factor contributing to this error. Nevertheless, the calculation error remained below 8%, indicating that this method was suitable for predicting V_{B}. The amount of hydrate in the sediment layer before gas flow has been determined. Assuming a uniform distribution of hydrate within the sediment layer, thus, the blockage location (X_{B}) can be calculated by Eq. (11):

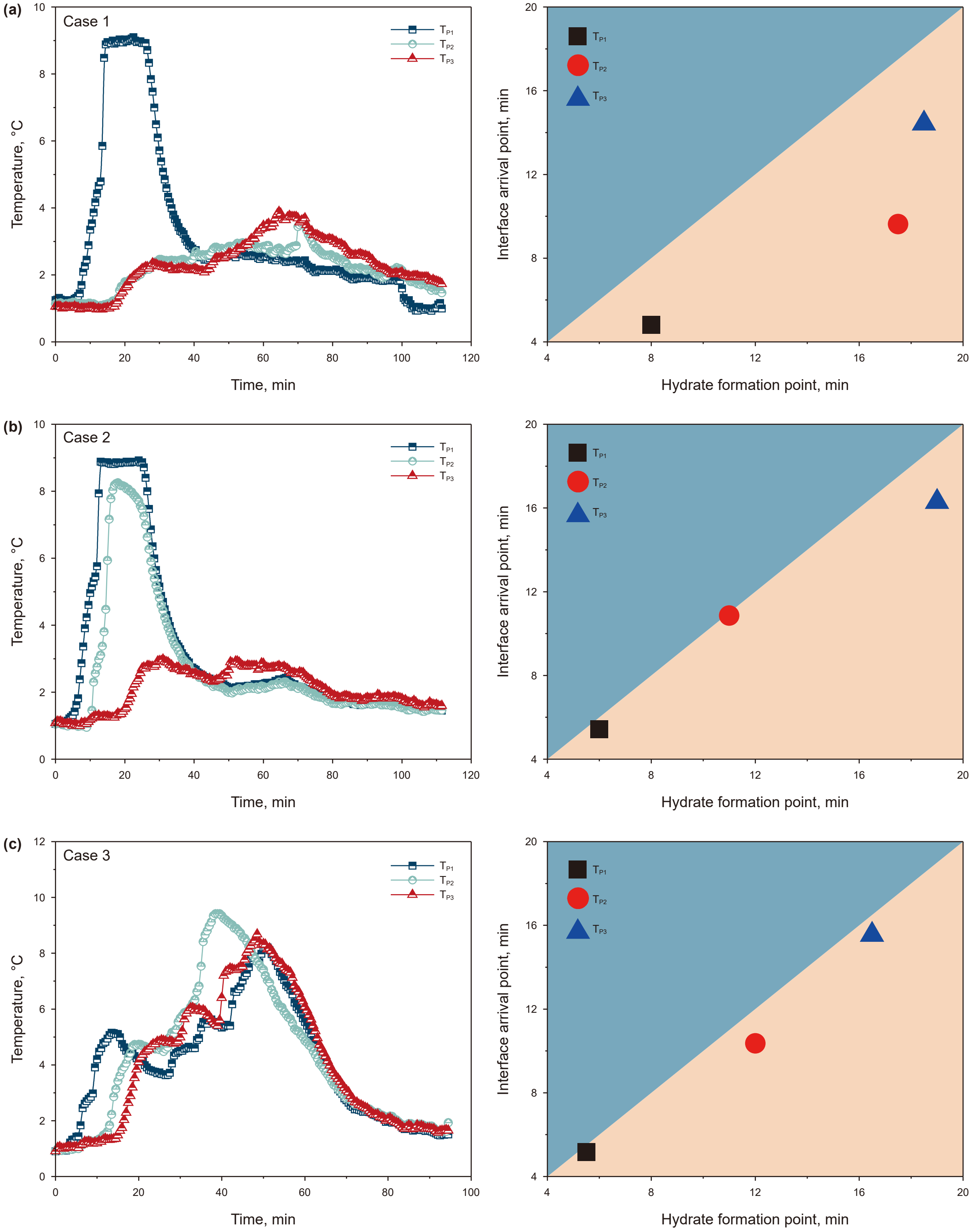

Fig. 10. Temperature changes and hydrate formation characteristics during gas flow process.

$$X_B = \frac{V_B}{V_P \cdot (1 - S_H)} \cdot L \tag{11}$$

where S_H is the average hydrate saturation before the gas flow process, %, the blockage interface in the vessel is demonstrated in Fig. 11. The calculation error was less than 8%, indicating that the model has good predictive accuracy. Zhang et al. (2019) proposed a hydrate blockage calculation model by integrating the hydrate stability zone prediction model, the hydrate formation prediction model, and the hydrate deposition prediction model, which required comprehensive consideration of hydrate phase change, wellbore structure, gas-phase enthalpy variation, and temperature-

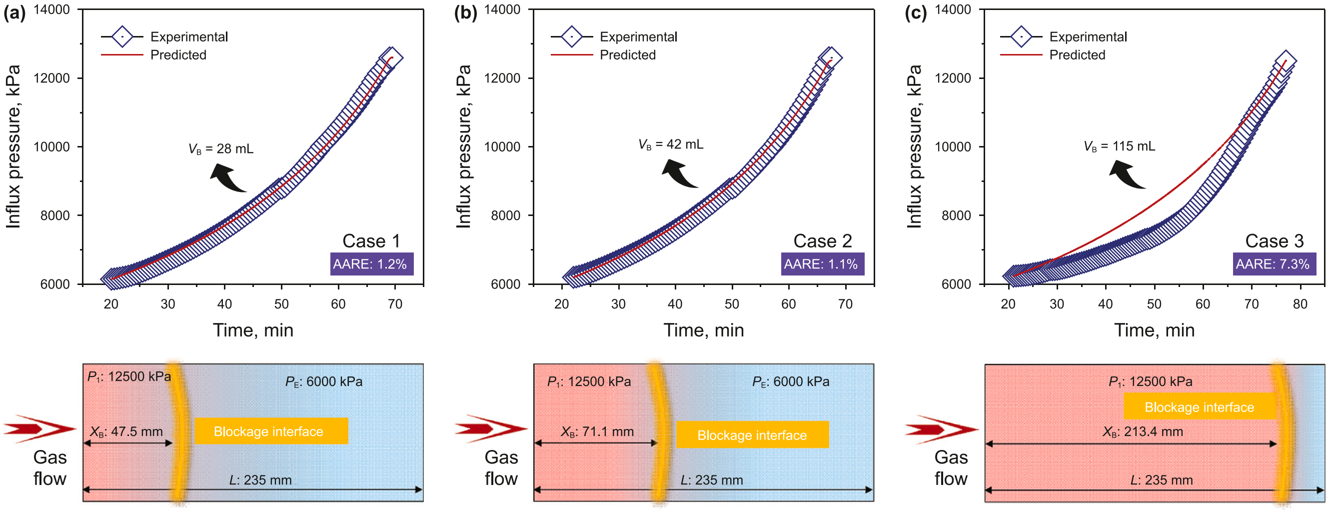

Fig. 11. Comparison of real-time influx pressure between actual values with expected values, and blockage interface distribution in Case 1 (**a**), Case 2 (**b**), Case 3 (**c**).

pressure changes, involving a large number of parameters. In contrast, the model proposed in this study can directly infer spatial distribution characteristics and predict blockage locations based on pressure evolution data, requiring fewer parameters and offering greater convenience for engineering applications. The model in this study provides a theoretical basis for determining blockage positions during the hydrate exploitation and pipeline transportation process and offers a theoretical foundation for the accumulation of natural gas hydrate in marine environment.

4. Conclusions

This study systematically investigates the evolution of methane hydrate formation, water flow, and gas flow in sediments with varying water distributions. The key findings are as follows:

(1) The real-time hydrate formation rate was found to be inversely proportional to the amount of hydrate formed. A hydrate formation model for gas-saturated systems was developed, achieving a prediction error of less than 9%. However, as a fundamental model, it still requires further refinement. Future research should investigate the influence of key formation factors on the parameters *r* and *K*, aiming to derive their mathematical expressions and improve the model's accuracy and applicability.
(2) Hydrate formation during the gas flow process occupied the pore space, which is the direct cause of the blockage effect in the sediment layer. Hydrate blockage occurred after gas displaces pore water, with observed pressure differences reaching up to 6500 kPa. This can potentially lead to local breakthrough phenomena and significant methane leakage. Increasing the number of production wells and implementing pressure reduction strategies during hydrate exploitation may help mitigate hydrate reformation induced by gas flow.
(3) A blockage localization model with an error of less than 8% was proposed to address the issue of pore blockage during gas flow. By analyzing pressure evolution, the blockage position can be calculated, providing a simple and efficient method for locating blockages in sediments and pipelines during oil and gas production. For this model, further pore-scale visualization validation and large-scale studies are still required to enhance its applicability.

CRediT authorship contribution statement

Guo-Jun Zhao: Writing – original draft, Methodology, Investigation, Funding acquisition, Formal analysis, Data curation. **Jia-Nan Zheng:** Writing – review & editing, Validation, Conceptualization. **Ming-Jun Yang:** Supervision, Project administration, Data curation. **Yong-Chen Song:** Funding acquisition, Data curation.

Declaration of competing interest

The authors declare that they have no known competing financial interests or personal relationships that could have appeared to influence the work reported in this paper.

Acknowledgements

This study was financially supported by the National Natural Science Foundation of China (524B2088, 52525602, 52306205), the National Key Research and Development Plan of China (2021YFC2800902), and the Fundamental Research Funds for the Central Universities in China (DUT21ZD103).

References

Bohrmann, G., Berndt, C., Lin, S., et al., 2023. Geological controls on the distribution of gas hydrates in the shallow parts of the gas hydrate stability zone–constraints from seafloor drilling off Taiwan. Mar. Petrol. Geol. 153, 106253. https://doi.org/10.1016/j.marpetgeo.2023.106253.
Chen, B.B., Sun, H.R., Li, K.H., et al., 2019. Experimental investigation of natural gas hydrate production characteristics via novel combination modes of depressurization with water flow erosion. Fuel 252, 295–303. https://doi.org/10.1016/j.fuel.2019.04.120.
Chen, B.B., Liu, Z.Y., Sun, H.R., et al., 2021. The synthetic effect of traditional-thermodynamic-factors (temperature, salinity, pressure) and fluid flow on natural gas hydrate recovery behaviors. Energy 233, 121147. https://doi.org/10.1016/j.energy.2021.121147.
Chibura, P.E., Zhang, W., Luo, A., et al., 2022. A review on gas hydrate production feasibility for permafrost and marine hydrates. J. Nat. Gas Sci. Eng. 100, 104441. https://doi.org/10.1016/j.jngse.2022.104441.
Dong, S., Zheng, J.N., Li, Q., et al., 2025. Decomposition thermokinetics and heat balance analysis of depressurized methane hydrate deposits under poor heat transfer conditions. Int. J. Heat Mass Tran. 238, 126480. https://doi.org/10.1016/j.ijheatmasstransfer.2024.126480.
Farhadian, A., Naeiji, P., Varfolomeev, M.A., et al., 2022. Reconsideration of the micellization theory: promotion or inhibition of gas hydrate formation for gas storage and flow assurance applications. Chem. Eng. J. 427, 131852. https://doi.org/10.1016/j.cej.2021.131852.

Feng, Y., Han, Y.Z., Jia, Y.X., et al., 2024. Visual study of methane hydrate kinetics in a microfluidic chip: effect of the resins extracted from the crude oil. Fuel 359, 130276. https://doi.org/10.1016/j.fuel.2023.130276.

Fu, X., Waite, W.F., Ruppel, C.D., 2021. Hydrate formation on marine seep bubbles and the implications for water column methane dissolution. J. Geophys. Res.: Oceans 126, e2021JC017363. https://doi.org/10.1029/2021JC017363.

Gong, G.J., Zhao, G.J., Pang, W.X., et al., 2023a. Review of hydrate-bearing sediment permeability for natural gas hydrate exploitation: measurement and application development. J. Petrol. Sci. Eng. 220, 111217. https://doi.org/10.1016/j.petrol.2022.111217.

Gong, G.J., Zhao, G.J., Pang, W.X., et al., 2023b. Continuous measurement of gas permeability in non-homogeneous hydrate reservoirs under effective pressure via a novel apparatus. Gas Sci. Eng. 118, 205091. https://doi.org/10.1016/j.jgsce.2023.205091.

Guo, Y., Li, S.X., Li, S.X., et al., 2025. Effect of interlayer flow capability on the interference of natural gas hydrate and shallow gas reservoir co-production. J. Clean. Prod. 493, 144996. https://doi.org/10.1016/j.jclepro.2025.144996.

Ji, Y.K., Hou, J., Zhao, E.M., et al., 2020. Study on the effects of heterogeneous distribution of methane hydrate on permeability of porous media using low-field NMR technique. J. Geophys. Res. Solid Earth 125, e2019JB018572. https://doi.org/10.1029/2019JB018572.

Ji, Y.K., Kneafsey, T.J., Hou, J., et al., 2022. Relative permeability of gas and water flow in hydrate-bearing porous media: a micro-scale study by lattice Boltzmann simulation. Fuel 321, 124013. https://doi.org/10.1016/j.fuel.2022.124013.

Kou, X., Feng, J.C., Li, X.S., et al., 2022. Memory effect of gas hydrate: influencing factors of hydrate reformation and dissociation behaviors. Appl. Energy 306, 118015. https://doi.org/10.1016/j.apenergy.2021.118015.

Lee, Y., Deusner, C., Kossel, E., et al., 2020. Influence of CH_4 hydrate exploitation using depressurization and replacement methods on mechanical strength of hydrate-bearing sediment. Appl. Energy 277, 115569. https://doi.org/10.1016/j.apenergy.2020.115569.

Li, K.H., Chen, B.B., Song, Y.C., et al., 2020. Molecular dynamics simulation of the effects of different thermodynamic parameters on methane hydrate dissociation: an analysis of temperature, pressure and gas concentrations. Fluid Phase Equilib. 516, 112606. https://doi.org/10.1016/j.fluid.2020.112606.

Li, S.G., Li, Y.J., Yang, L.B., et al., 2019. Prediction of phase equilibrium of methane hydrate below 272.2 K based on different equations of state. Fluid Phase Equilib. 490, 61–67. https://doi.org/10.1016/j.fluid.2018.12.026.

Li, Y.H., Tian, B.Y., You, Z.S., et al., 2025. Particle-scale study of the mechanical properties of sandy hydrate-bearing sediments using DEM combined with CT images. Energy 320, 135319. https://doi.org/10.1016/j.energy.2025.135319.

Lv, X.F., Chen, S.K., Liu, Y., et al., 2025. Intelligent prediction of hydrate induction time in oil–water emulsion system based on data-driven and driving force. Chem. Eng. Sci. 307, 121305. https://doi.org/10.1016/j.ces.2025.121305.

Ma, S.H., Liu, Z.Y., Zheng, J.N., et al., 2024. Natural gas hydrate decomposition characteristics at the exploitation anaphase via sediment warming. Energy Fuels. 38, 14334–14342. https://doi.org/10.1021/acs.energyfuels.4c02709.

Marques, D.C., Bassani, C.L., Kakitani, C., Morales, R.E., et al., 2022. Mapping wall deposition trends of gas hydrates: I. gas-water-hydrate systems. Ind. Eng. Chem. Res. 61, 2333–2345. https://doi.org/10.1021/acs.iecr.1c04723.

Ren, J.F., Cheng, C., Xiong, P.F., et al., 2022. Sand-rich gas hydrate and shallow gas systems in the Qiongdongnan Basin, northern South China Sea. J. Petrol. Sci. Eng. 215, 110630. https://doi.org/10.1016/j.petrol.2022.110630.

Sakurai, S., Hoskin, B., Choi, J., et al., 2021. Investigating hydrate formation rate and the viscosity of hydrate slurries in water-dominant flow: flowloop experiments and modelling. Fuel 292, 120193. https://doi.org/10.1016/j.fuel.2021.120193.

Song, Y.C., Wang, P.F., Jiang, L.L., et al., 2015. Methane hydrate formation/reformation in three experimental modes: a preliminary investigation of blockage prevention during exploitation. J. Nat. Gas Sci. Eng. 27, 1814–1820. https://doi.org/10.1016/j.jngse.2015.11.009.

Song, Y.C., Tian, M.R., Zheng, J.N., et al., 2022. Thermodynamics analysis and ice behavior during the depressurization process of methane hydrate reservoir. Energy 250, 123801. https://doi.org/10.1016/j.energy.2022.123801.

Sun, H.R., Chen, B.B., Li, K.H., et al., 2023. Methane hydrate re-formation and blockage mechanism in a pore-level water-gas flow process. Energy 263, 125851. https://doi.org/10.1016/j.energy.2022.125851.

Sun, H.R., Chen, B.B., Yang, M.J., 2020a. Effect of multiphase flow on natural gas hydrate production in marine sediment. J. Nat. Gas Sci. Eng. 73, 103066. https://doi.org/10.1016/j.jngse.2019.103066.

Sun, H.R., Chen, B.B., Zhao, G.J., et al., 2020b. The enhancement effect of water-gas two-phase flow on depressurization process: important for gas hydrate production. Appl. Energy 276, 115559. https://doi.org/10.1016/j.apenergy.2020.115559.

Sun, L.J., Wang, T., Dong, B., et al., 2021. Pressure oscillation controlled CH_4/CO_2 replacement in methane hydrates: CH_4 recovery, CO_2 storage, and their characteristics. Chem. Eng. J. 425, 129709. https://doi.org/10.1016/j.cej.2021.129709.

Wang, J.Q., Ma, F., Bouri, E., et al., 2022. Volatility of clean energy and natural gas, uncertainty indices, and global economic conditions. Energy Econ. 108, 105904. https://doi.org/10.1016/j.eneco.2022.105904.

Wang, P.F., Wang, S.L., Song, Y.C., et al., 2018. Dynamic measurements of methane hydrate formation/dissociation in different gas flow direction. Appl. Energy 227, 703–709. https://doi.org/10.1016/j.apenergy.2017.08.056.

Wang, P.F., Yang, M.J., Chen, B.B., et al., 2017. Methane hydrate reformation in porous media with methane migration. Chem. Eng. Sci. 168, 344–351. https://doi.org/10.1016/j.ces.2017.04.036.

Wang, Z.H., Wan, Y.Z., Zhang, Y.C., et al., 2024. Gas and water relative permeability in THF hydrate-bearing Berea sandstone. Energy Fuels. 38, 11706–11716. https://doi.org/10.1021/acs.energyfuels.4c01402.

Wei, R.P., Xia, Y.Q., Wang, Z.F., et al., 2022a. Long-term numerical simulation of a joint production of gas hydrate and underlying shallow gas through dual horizontal wells in the South China Sea. Appl. Energy 320, 119235. https://doi.org/10.1016/j.apenergy.2022.119235.

Wei, W.N., Li, B., Gan, Q., et al., 2022b. Research progress of natural gas hydrate exploitation with CO_2 replacement: a review. Fuel 312, 122873. https://doi.org/10.1016/j.fuel.2021.122873.

Xu, R., Kou, X., Wu, T.W., et al., 2023. Pore-scale experimental investigation of the fluid flow effects on methane hydrate formation. Energy 271, 126967. https://doi.org/10.1016/j.energy.2023.126967.

Yang, M.J., Song, Y.C., Jiang, L.L., et al., 2015. Behaviour of hydrate-based technology for H_2/CO_2 separation in glass beads. Separ. Purif. Technol. 141, 170–178. https://doi.org/10.1016/j.seppur.2014.11.019.

Ye, H.Y., Zhang, Q., Yao, Y.X., et al., 2025. Co-production of gas hydrates, shallow gas, and deep gas in the Qiongdongnan Basin: a pathway to commercial production. Appl. Energy 384, 125482. https://doi.org/10.1016/j.apenergy.2025.125482.

Yin, Z., Khurana, M., Tan, H.K., et al., 2018. A review of gas hydrate growth kinetic models. Chem. Eng. J. 342, 9–29. https://doi.org/10.1016/j.cej.2018.01.120.

Yu, Y.S., Zhang, X., Liu, J.W., et al., 2021. Natural gas hydrate resources and hydrate technologies: a review and analysis of the associated energy and global warming challenges. Energy Environ. Sci. 14, 5611–5668. https://doi.org/10.1039/d1ee02093e.

Zhang, J.D., Liu, X.H., Chen, D.Y., et al., 2022. An investigation on the permeability of hydrate-bearing sediments based on pore-scale CFD simulation. Int. J. Heat Mass Tran. 192, 122901. https://doi.org/10.1016/j.ijheatmasstransfer.2022.122901.

Zhang, J.B., Wang, Z.Y., Sun, B.J., et al., 2019. An integrated prediction model of hydrate blockage formation in deep-water gas wells. Int. J. Heat Mass Tran. 140, 187–202. https://doi.org/10.1016/j.ijheatmasstransfer.2019.05.039.

Zhang, J.B., Zhang, N.T., Sun, X.H., et al., 2023a. Pore-scale investigation on methane hydrate formation and plugging under gas–water flow conditions in a micromodel. Fuel 333, 126312. https://doi.org/10.1016/j.fuel.2022.126312.

Zhang, J.B., Wang, Z.Y., Lou, W.Q., et al., 2023b. Research on methane hydrate formation in porous media with gas–water two-phase flow. Gas Sci. Eng. 110, 204898. https://doi.org/10.1016/j.jgsce.2023.204898.

Zhang, Y.C., Liu, L.L., Li, J., et al., 2024a. The pore-structure characteristics of foraminiferal shells and their relations with natural gas hydrate formation in the marine sediments. Gas Sci. Eng. 124. https://doi.org/10.1016/j.jgsce.2024.205257.

Zhang, Y.C., Liu, L.L., Sun, J., et al., 2024b. Application of time domain reflectometry to triaxial shear tests on hydrate-bearing sediments. Measurement 238. https://doi.org/10.1016/j.measurement.2024.115369.

Zhang, Z., Liu, L.L., Lu, W.J., et al., 2023c. Permeability of hydrate-bearing fine-grained sediments: research status, challenges and perspectives. Earth Sci. Rev. 244, 104517. https://doi.org/10.1016/j.earscirev.2023.104517.

Zhao, G.J., Yang, M.J., Lv, X., et al., 2023a. MRI insight on multiphase flow in hydrate-bearing sediment and development mechanism of hydrate seal. Pet. Sci. 20, 3854–3864. https://doi.org/10.1016/j.petsci.2023.07.017.

Zhao, G.J., Gong, G.J., Sun, H.R., et al., 2022a. Effect of methane solubility on hydrate formation and dissociation: review and perspectives. Energy Fuels. 36, 7269–7283. https://doi.org/10.1021/acs.energyfuels.2c01017.

Zhao, G.J., Zheng, J.N., Gong, G.J., et al., 2023b. Formation characteristics and leakage termination effects of CO_2 hydrate cap in case of geological sequestration leakage. Appl. Energy 351, 121896. https://doi.org/10.1016/j.apenergy.2023.121896.

Zhao, G.J., Yang, M.J., Pang, W.X., et al., 2022b. Effects of hydrate cap on leakage prevention and capacity improvement of sub-seabed CO_2 sequestration. Chem. Eng. J. 450, 138493. https://doi.org/10.1016/j.cej.2022.138493.

Zhao, G.J., Zheng, J.N., Gong, G.J., et al., 2025a. Production characteristics and visualization insight of top/bottom depressurization exploitation of natural gas hydrate with overpressure gas. Fuel 379, 133030. https://doi.org/10.1016/j.fuel.2024.133030.

Zhao, J., Wang, B., Sum, A.K., 2017. Dynamics of hydrate formation and deposition under pseudo multiphase flow. AIChE J. 63, 4136–4146. https://doi.org/10.1002/aic.15722.

Zhao, Q., Li, X.S., Chen, Z.Y., et al., 2025b. Dynamic competitive co-production behaviors between natural gas hydrate and higher-pressure shallow gas under wellbore interference: an experimental study. Appl. Energy 384, 125474. https://doi.org/10.1016/j.apenergy.2025.125474.

Zheng, J.N., Yang, M.J., 2019. Phase equilibrium data of CO_2-MCP hydrates and CO_2 gas uptake comparisons with CO_2-CP hydrates and CO_2-C_3H_8 hydrates. J. Chem. Eng. Data 64, 372–379. https://doi.org/10.1021/acs.jced.8b00893.